Polyharmonic Spline Modelling of Tissue Deformation for Ultrasound-Guided Surgery

Kian Zalzalah, Alec Cotton, and Carlos Rossa
Department of Systems and Computer Engineering
Carleton University, Ottawa, ON, Canada
{kianzalzalah, aleccotton}@cmail.carleton.ca; carlosrossa@cunet.carleton.ca

***Abstract*—Ultrasound-guided percutaneous surgery simulation requires tissue deformation models that update in real-time as surgical tools move through the tissue. Standard methods often rely on finite element modelling, but these models are computationally demanding for interactive and portable simulators. In this paper, we present a volumetric tissue deformation model based on three-dimensional (3D) polyharmonic splines (PHS) as an efficient alternative to simulate tissue deformation in real-time.**

In the proposed algorithm, the tissue is discretized into a finite mesh of points. Tool/tissue friction and tissue cutting are modelled as a distance-decaying displacement field that generates forward nodal offsets in the mesh with rigid boundary anchors included to prevent drift and enforce stable deformation under repeated updates. A 3D PHS interpolant then propagates these local displacements smoothly to all mesh points, yielding a continuous volumetric deformation field that can be sampled on arbitrary planes for ultrasound image rendering. Compared against a finite element model, the results show that while both models show small discrepancies in terms of nodal displacement, the proposed PHS algorithm is 410 times faster on a 150,000 node mesh. The proposed framework produces stable and visually realistic deformations at interactive update rates, demonstrating strong potential for integration into real-time, haptics-enabled ultrasound training simulators.

I. Introduction

Minimally invasive surgery (MIS) enables diagnostic and interventional procedures to be performed through small incisions rather than large surgical openings. By reducing tissue trauma, blood loss, post-operative pain, and recovery time, MIS has become the preferred approach across a wide range of interventions, including biopsies, ablation therapies, and urological procedures. Unlike open surgery, where anatomical structures are directly visible and accessible, MIS relies heavily on indirect visualization of the tissue through internal cameras or external imaging. Surgeons must operate with a limited field of view, reduced depth perception, and constrained tool motion, all while maintaining the tool and target in the field of view. Ultrasound imaging is widely used due to its real-time capability, portability, and absence of ionizing radiation, making it especially suitable for repeated use and for vulnerable patient populations such as paediatrics.

In ultrasound-guided percutaneous surgery (usPS), when a tool is inserted into soft tissue it displaces and deforms the surrounding anatomy, shifts targets from their original locations, and compresses or stretches tissue layers. Such volumetric deformations are partially observed in two-dimensional (2D) ultrasound images and directly affect how the tool and tissue appear in the images. In addition, the tool shaft produces extended hyperechoic traces in the images, further complicating the procedure [1]–[3]. Maintaining continuous tool and target visibility requires frequent probe motion, while simultaneously advancing and steering the tool. This bimanual coordination is a well-known source of a steep learning curve in ultrasound-guided interventions. In percutaneous nephrolithotomy, for example, proficiency can require up to 60 trials, with expert performance only reached beyond 100 trials [4]–[6].

Virtual and cyber-physical simulators are increasingly used in training programs to train clinicians and overcome learning curves. Surgical simulators give the trainee the ability to practice their skills in a virtual environment that can be programmed and changed easily to mimic specific cases [7]. Many of these simulators model the tool's interaction with the tissue to update the simulated ultrasound images in real-time, with the goal of teaching the trainee how to interpret images and minimize damage done to surrounding structures during surgery [8], [9].

Finite element modelling (FEM) is widely used to predict soft-tissue deformation under tool loading by discretizing continuum mechanics models into large finite systems that incorporate material properties and boundary conditions. FEM models have been reported for needle insertion and guidance in liver interventions [10], [11], needle steering in brachytherapy [8], [12], and non-rigid image deformation [13], [14]. For real-time simulation, however, the model must be calculated repeatedly as the needle advances, which becomes computationally expensive for volumetric meshes with high spatial resolution [15], [16]. In addition, selecting tissue parameters and maintaining numerical stability in scenarios involving nonlinearity or large deformations can be challenging in practice [17]. Despite continued progress in computing and solver technology, these factors limit the portability achievable with FEM in simulators.

In our prior work, we showed that thin plate spline (TPS) can predict 2D soft tissue deformation during usPS with an accuracy comparable to that of an equivalent FEM model, but with lower computational cost [18]. Spline-based models represent non-rigid motion by prescribing a set of source and target mesh landmark correspondences and computing a smooth interpolant that propagates these constraints to all remaining points. Compared with FEM solvers, these models avoid explicitly solving partial differential equations

and instead produce a globally regularized deformation field from a compact set of constraints, making them attractive for interactive simulation [19]. A major limitation of our past work is that the proposed model was limited to deformations along a single 2D plane and could not enforce volumetric coherence of deformations driven by a 3D tool-tissue interaction.

The proposed method is therefore intended as a fast surrogate deformation model for interactive simulation rather than a full constitutive tissue model. Rather than treating deformation as an image registration problem, the proposed method generates spline constraints directly from needle–tissue interaction mechanisms in a 3D mesh. It captures the effect of tissue displacement due to friction along the needle shaft and tissue cutting at the needle tip; effects that are converted into localized nodal displacements within the mesh. These displacements serve as inputs to a 3D PHS model, which smoothly propagates deformation throughout the mesh volume while enforcing boundary conditions. The proposed framework enables consistent volumetric deformation and supports arbitrary planar slicing of the deformed volume, which is essential for realistic ultrasound image simulation. The resulting approach avoids explicit force-based FEM formulations, reduces computational complexity, and provides stable, visually realistic deformation suitable for real-time surgical simulation.

Section II introduces the PHS formulation, followed in Section III by a description of how tool/tissue interaction is integrated into the model. The results reported in Section IV show that on a 150,000 node mesh, the proposed method is 410 times faster than a standard FEM model (FEniCSx) while achieving minimal mesh deformation discrepancy. The results are followed by a discussion and the paper concludes with outlines of future work.

II. Polyharmonic Spline-Based Tissue Deformation

The proposed three-dimensional PHS formulation is the direct analogue of the 2D TPS landmark-interpolation, as in our previous work [18], extended to 3D. The tissue is represented as a volumetric mesh of N discrete points $\boldsymbol{\zeta}_s(x, y, z) \in \mathbb{R}^3$, where (x, y, z) denote the spatial coordinates of each point in the undeformed volume. These points are uniformly spaced by k in all three directions. For example, a point located one unit forward along the x-axis from the origin has coordinates $\boldsymbol{\zeta}_s(k, 0, 0)$.

Consider a second volume in which a point i is displaced from its original position $\boldsymbol{\zeta}_{s_i}(x, y, z)$ to a new coordinate $\boldsymbol{\zeta}_{t_i}(x, y, z)$. The objective of PHS is to determine a transformation $g(x, y, z) \in \mathbb{R}^3$ that deforms the original volume such that a source point $\boldsymbol{\zeta}_{s_i}(x, y, z)$ is mapped to a corresponding target point $\boldsymbol{\zeta}_{t_i}(x, y, z)$, while minimizing the bending energy of the whole mesh. This process is illustrated in Fig.1, where points in the source configuration are displaced to new target locations.

Unlike continuum-based approaches that explicitly solve governing equations of tissue mechanics, the proposed method enforces smoothness through a polyharmonic spline interpolant in $\mathbb{R}^3$. Input nodal displacements, derived from needle-tissue interaction (described later in Sec. III), are prescribed at a sparse set of mesh point displacements, and the deformation of the remaining points is obtained by smoothly interpolating these constraints over the mesh.

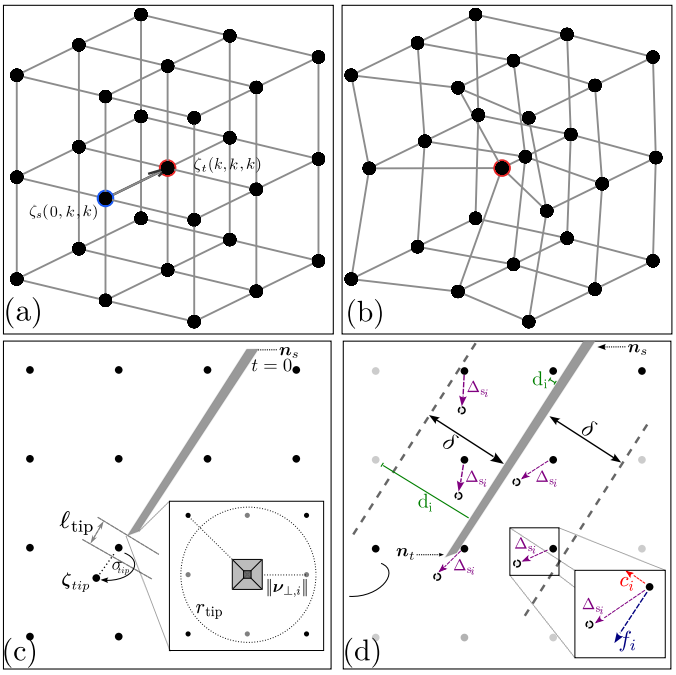

Fig. 1. a) Volumetric mesh of points describing source points $\boldsymbol{\zeta}_s(x, y, z)$ displaced to a target point $\boldsymbol{\zeta}_t(x, y, z)$. b) Resulting deformation of the mesh. c) Out-of-plane view showing nodes affected by tissue cutting at the needle tip. d) In-plane view showing axial and lateral displacement of nodes affected by friction along the shaft.

Given the set of volumetric mesh points $\boldsymbol{\zeta}_s(x, y, z) \in \mathbb{R}^3$, our algorithm first computes target positions $\boldsymbol{\zeta}_{t_i}$ for a subset of points selected as interpolation landmarks. These landmarks include n points experiencing non-zero displacement due to needle-tissue friction, tissue displacement at the needle tip, and rigidly pinned boundary points. The deformation mapping $g : \mathbb{R}^3 \to \mathbb{R}^3$ is defined as

$$g(x, y, z) = \mathbf{a}_0 + \mathbf{a}_1 x + \mathbf{a}_2 y + \mathbf{a}_3 z + \sum_{j=1}^{n} \mathbf{w}_j \, U(r_{ij}), \quad (1)$$

where $\mathbf{a}_0, \ldots, \mathbf{a}_3 \in \mathbb{R}^3$ are affine coefficient vectors to be determined, and $\mathbf{w}_j \in \mathbb{R}^3$ are spline weights given to the j^{th} landmark point $\boldsymbol{\zeta}_{s_j}$. The pairwise Euclidean distance is

$$r_{ij} = \left\| \boldsymbol{\zeta}_{s_i} - \boldsymbol{\zeta}_{s_j} \right\|. \quad (2)$$

In $\mathbb{R}^3$, we adopt the lowest-order polyharmonic kernel,

$$U(r_{ij}) = r_{ij}. \quad (3)$$

This choice yields a smooth volumetric deformation field while remaining numerically stable for repeated evaluation.

Using the n landmark points, a symmetric kernel matrix $\mathbf{K} \in \mathbb{R}^{n\times n}$ is constructed as

$$\mathbf{K} = \begin{bmatrix} \epsilon & U(r_{12}) & \cdots & U(r_{1n}) \\ U(r_{21}) & \epsilon & \cdots & U(r_{2n}) \\ \vdots & \vdots & \ddots & \vdots \\ U(r_{n1}) & U(r_{n2}) & \cdots & \epsilon \end{bmatrix}, \tag{4}$$

where $\epsilon > 0$ is a small fixed diagonal regularization constant used to improve numerical conditioning. To incorporate affine behaviour, a matrix of landmark source points $\mathbf{R} \in \mathbb{R}^{n\times 4}$ is constructed by concatenating the n landmark coordinates with a column of ones:

$$\mathbf{R} = \begin{bmatrix} 1 & 1 & \dots & 1 \\ \boldsymbol{\zeta}_{s_1} & \boldsymbol{\zeta}_{s_2} & \dots & \boldsymbol{\zeta}_{s_n} \end{bmatrix}^T, \tag{5}$$

where $\boldsymbol{\zeta}_{s_j} = [x_j \ y_j \ z_j]^T$ denotes the j^{th} landmark point in the source configuration. To solve for the interpolation coefficient, we first assemble the matrices above as

$$\mathbf{L} = \begin{bmatrix} \mathbf{K} & \mathbf{R} \\ \mathbf{R}^T & \mathbf{0}_{4\times 4} \end{bmatrix}, \tag{6}$$

where $\mathbf{0}_{4\times 4}$ is matrix of zeros associated with the affine side constraints of the PHS. Note that $\mathbf{L} \in \mathbb{R}^{(n+4)\times(n+4)}$ depends on the number of active landmarks n, not on the total mesh size. The spline weight vectors and affine coefficient vectors can now be obtained by solving

$$\mathbf{L}\begin{bmatrix} \mathbf{w}_1 & \dots & \mathbf{w}_n & \mathbf{a}_0 & \mathbf{a}_1 & \mathbf{a}_2 & \mathbf{a}_3 \end{bmatrix}^T = \begin{bmatrix} \boldsymbol{\zeta}_{t_1} \\ \vdots \\ \boldsymbol{\zeta}_{t_n} \\ \mathbf{0}_{4\times 3} \end{bmatrix}, \tag{7}$$

which enforces exact interpolation of the landmark target positions while satisfying the affine constraints of the PHS model. Once the spline parameters are obtained, the deformed position of any mesh point $\boldsymbol{\zeta}_{s_i}$ is computed by evaluating (1) at its spatial coordinates:

$$\boldsymbol{\zeta}'_{s_i} = \mathbf{a}_0 + \mathbf{a}_1 x_i + \mathbf{a}_2 y_i + \mathbf{a}_3 z_i + \sum_{j=1}^{n} \mathbf{w}_j \left\| \boldsymbol{\zeta}_{s_i} - \boldsymbol{\zeta}_{s_j} \right\|. \tag{8}$$

The deformation can be efficiently evaluated for all mesh points and updated incrementally as the needle advances through the tissue volume.

Algorithm 1 Incremental 3D PHS Deformation

```
Initialize volumetric source mesh points ζ_s(x, y, z)
while needle advances do
    Get target positions ζ_{t_i} from needle/tissue interaction
    Select n active landmark points {ζ_{s_j}}_{j=1}^n
    Construct K using (4)
    Construct R using (5)
    Assemble L using (6)
    Solve for {w_j}_{j=1}^n and {a_ℓ}_{ℓ=0}^3 using (7)
    Deform mesh points ζ_{s_i} using (8) to obtain ζ'_{s_i}
    Update mesh: ζ_s ← ζ'_s
end while
```

III. Needle-Tissue Interaction Model

The needle-tissue interaction model generates physically motivated mesh displacements that capture the dominant effects of needle insertion. These localized displacements are subsequently used as interpolation constraints in the PHS algorithm described earlier. The needle is modelled as a rigid instrument with zero width that enters the tissue volume at a fixed entry point $\mathbf{n}_s$. If the needle tip position in the tissue is $\mathbf{n}_t$, a point on the needle shaft can be modelled by a straight line parameterized as

$$\mathbf{n}(t) = \mathbf{n}_s + t(\mathbf{n}_t - \mathbf{n}_s), \qquad 0 \le t \le 1, \tag{9}$$

where t denotes the normalized position along the shaft. Assuming that the needle only moves along the direction of its shaft and not sideways, the unit vector given the insertion direction is

$$\hat{\mathbf{u}} = \frac{\mathbf{n}_t - \mathbf{n}_s}{\|\mathbf{n}_t - \mathbf{n}_s\|}. \tag{10}$$

For each mesh point $\boldsymbol{\zeta}_{s_i}$, we compute the projection along the needle of its distance to the needle's entry point in the tissue

$$\tau_i = (\boldsymbol{\zeta}_{s_i} - \mathbf{n}_s) \cdot \hat{\mathbf{u}}, \tag{11}$$

from which the closest point from $\boldsymbol{\zeta}_{s_i}$ to the shaft line is

$$\mathbf{p}_i = \mathbf{n}_s + \tau_i \, \hat{\mathbf{u}}. \tag{12}$$

and the shortest d_i distance between mesh point $\boldsymbol{\zeta}_{s_i}(x, y, z)$ and the needle shaft is given as

$$d_i = \|\boldsymbol{\zeta}_{s_i} - \mathbf{p}_i\|. \tag{13}$$

Needle-tissue interaction is modelled as the superposition of two dominant effects: friction drags mesh points along the insertion direction around the needle shaft, and needle insertion pushes mesh points ahead of the needle tip.

A. Tool-Tissue Friction Along the Needle Shaft

We assume that the needle shaft friction affects mesh points within a tunable radius δ, that is, if $d_i \le \delta$. Points within this region are subject to two friction-associated effects: (i) axial drag along the insertion direction, and (ii) inward pull toward the shaft.

The axial drag, i.e., the induced displacement of a mesh point i in the direction of $\hat{\mathbf{u}}$ is modelled as:

$$f_i = f_{\max} e^{\left(-\frac{d_i^2}{2\sigma_s^2}\right)}, \qquad d_i \le \delta, \tag{14}$$

where $f_{\max}$ is the maximum shaft-induced displacement and σ_s is a tunable parameter that controls how the drag decays exponentially as the distance to the shaft increases.

The shaft locally pulls the tissue toward the needle. We define the inward radial unit vector

$$\hat{\mathbf{r}}_i = -\frac{\boldsymbol{\zeta}_{s_i} - \mathbf{p}_i}{\|\boldsymbol{\zeta}_{s_i} - \mathbf{p}_i\|}, \tag{15}$$

and prescribe an inward pull magnitude c_i with similar radial decay,

$$c_i = \gamma_{\max} e^{\left(-\frac{d_i^2}{2\sigma_c^2}\right)}, \qquad d_i \le \delta, \tag{16}$$

where $\gamma_{\max}$ sets the maximum inward pull and σ_c controls its radial extent decay. The total shaft-induced displacement of a mesh point is then the superposition of the two effects, that is:

$$\boldsymbol{\Delta}_{s_i} = f_i\,\hat{\mathbf{u}} + c_i\,\hat{\mathbf{r}}_i, \qquad d_i \le \delta. \tag{17}$$

For points satisfying $d_i > \delta$ we set $\boldsymbol{\Delta}_{s_i} = \mathbf{0}$. The updated target position for each affected point is therefore

$$\boldsymbol{\zeta}_{t_i} = \boldsymbol{\zeta}_{s_i} + \boldsymbol{\Delta}_{s_i}. \tag{18}$$

B. Tissue Displacement due to Needle Cutting at the Tip

The needle cuts and compresses tissue directly ahead of its tip, located at $\mathbf{n}_t$. To capture this effect, we define a cylindrical region aligned with the needle shaft ahead of the tip. For each mesh point $\boldsymbol{\zeta}_{s_i}$, let $\boldsymbol{\nu}_i = \boldsymbol{\zeta}_{s_i} - \mathbf{n}_t$ denote the vector connecting the needle tip to a mesh point. A mesh point $\boldsymbol{\zeta}_{s_i}$ is considered to be influenced by the needle tip if the point within a distance ℓ_{tip} in front of the tip, that is:

$$0 < \boldsymbol{\nu}_i \cdot \hat{\mathbf{u}} \le \ell_{\text{tip}}. \tag{19}$$

Next, we decompose $\boldsymbol{\nu}_i$ into components parallel and perpendicular to the needle axis $\hat{\mathbf{u}}$. The parallel component is the projection $\boldsymbol{\nu}_{\parallel,i} = (\boldsymbol{\nu}_i \cdot \hat{\mathbf{u}})\hat{\mathbf{u}}$, and subtracting it yields the perpendicular component $\boldsymbol{\nu}_{\perp,i} = \boldsymbol{\nu}_i - \boldsymbol{\nu}_{\parallel,i}$. The norm $\|\boldsymbol{\nu}_{\perp,i}\|$ is the shortest radial distance from $\boldsymbol{\zeta}_{s_i}$ to the needle axis. We therefore require

$$\|\boldsymbol{\nu}_{\perp,i}\| \le r_{\text{tip}}. \tag{20}$$

for a mesh point to be affected by tissue cutting, with r_{tip} denoting the maximum radial distance from the needle tip. For points satisfying (19)–(20), we define the tip-induced target position as $\boldsymbol{\zeta}_{t_{\text{tip}_i}}$.

$$\boldsymbol{\zeta}_{tip_i} = \boldsymbol{\zeta}_{s_i} + \sigma_{\text{tip}}\,\hat{\mathbf{u}}. \tag{21}$$

Once the required displacement of mesh points affected by the needle are defined, the position of all other mesh points can be calculated following Algorithm 1.

IV. Validation Against FEM

To quantitatively evaluate the accuracy of the proposed PHS model, its predicted mesh displacement is compared against a FEM reference simulation. Both models are defined on equivalent volumetric meshes, ensuring a one-to-one spatial match between points in the FEM and PHS meshes. The FEM engine used in this study is implemented using the FEniCSx computational framework [20]. FEniCSx provides a high-level, open-source environment for solving partial differential equations using variational formulations, making it well-suited for modelling soft tissue deformation under external loading conditions such as needle insertion.

In the proposed evaluation, the tissue domain is discretized into a volumetric finite element mesh, and tissue deformation is computed by solving the linear elasticity equations under quasi-static conditions. Needle–tissue interaction is modelled by applying localized forces and displacement constraints corresponding to shaft friction and compressive loading at the needle tip [8].

TABLE I
PHS tunable parameters selected via three-objective Non-dominated Sorting Genetic Algorithm II (NSGA-II) to minimize error with FEM simulation.

Parameter	Variable	Value
Maximum frictional displacement	$f_{\max}$	0.0227
Maximum inward radial shaft pull	$\gamma_{\max}$	0.0041
Distance in which shaft effects are truncated	σ_c	0.3873
Distance to capture points (friction)	σ_s	0.1291
Tip push effect magnitude	σ_{tip}	0.0266
Radial threshold to needle tip	r_{tip}	1.3185
Threshold to needle tip	ℓ_{tip}	2.1566

All simulations are performed in a normalized coordinate system. Specifically, the tissue volume is defined on a unit cube domain in $\mathbb{R}^3$, and the needle entry and target positions are specified in these normalized coordinates. This normalization enables consistent boundary conditions and insertion trajectories across evaluation scenarios, and allows mesh resolution to be varied without changing the underlying geometry. To study discretization effects, multiple FEM mesh densities are generated by varying the number of subdivisions along each axis; however, the domain size, needle path, and boundary constraints remain identical in the normalized space.

Before comparing the two models, the PHS must be tuned so that its predictions approach that of the FEM model. Let $\boldsymbol{\zeta}_i^{\text{FEM}} \in \mathbb{R}^3$ and $\boldsymbol{\zeta}_i^{\text{PHS}} \in \mathbb{R}^3$ denote the deformed positions of the i^{th} mesh point obtained from the FEM and PHS simulations, respectively. The point-wise displacement error for point i is defined as the Euclidean distance between the two predictions:

$$\epsilon_i = \left\| \boldsymbol{\zeta}_i^{\text{PHS}} - \boldsymbol{\zeta}_i^{\text{FEM}} \right\|. \tag{22}$$

The overall discrepancy between the two methods is computed over the set of N_a points experiencing non-zero deformation. Specifically, the mean absolute error (MAE) and root mean square error (RMSE) are defined as

$$MAE = \frac{1}{N_a}\sum_{i=1}^{N_a}\epsilon_i, \qquad RMSE = \sqrt{\frac{1}{N_a}\sum_{i=1}^{N_a}\epsilon_i^2}, \tag{23}$$

The $N - N_a$ points that remain rigidly fixed due to boundary conditions, or experience no displacement, are excluded from the error computation to avoid biasing the metrics toward zero.

The PHS model has 7 physically motivated application-dependent parameters that can be tuned; these are summarized in Table I. To find the set of parameters that minimize the MAE between the FEM and PHS simulations, we use a multiobjective, multivariable Non-dominated Sorting Genetic Algorithm II (NSGA-II) [21]. The MAE error is computed for three different simulations carried out in the same manner in

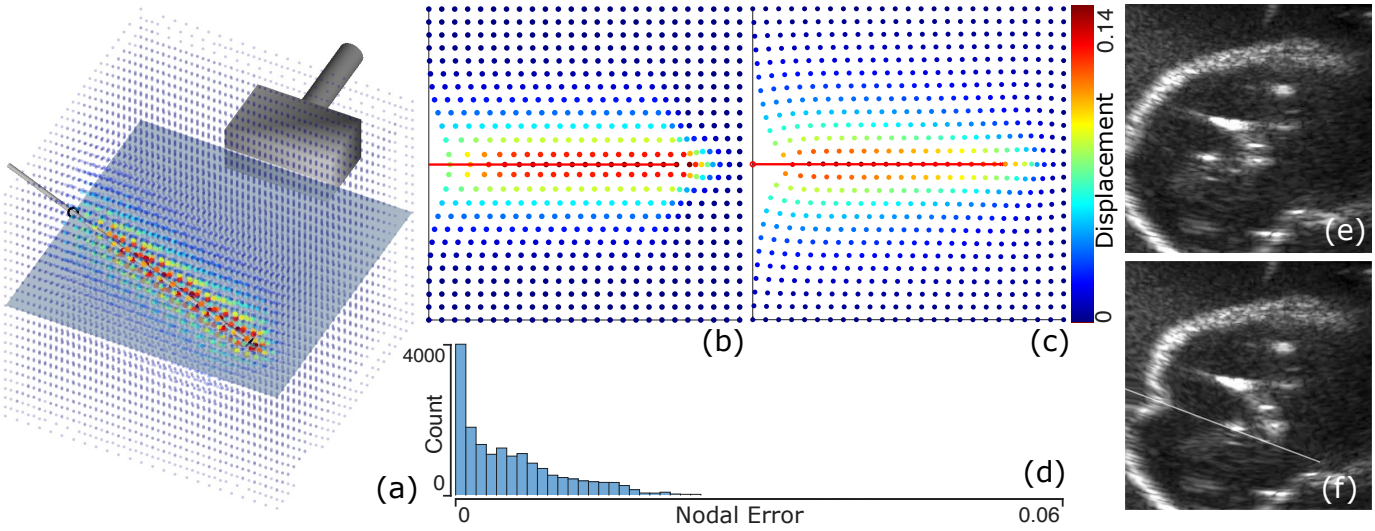

Fig. 2. Sample results. Fig. (a) shows a needle inserted in the mesh from the left side, and the corresponding mesh deformation calculated with PHS. The mesh can be sliced along any imaging plane, such as the blue plane at $z = 0.5$. Fig. (b) and (c) are two slices of a different volume calculated with PHS and FEM. The red line represents the needle. In (d) a histogram of absolute nodal error between PHS and FEM displacements from volumes corresponding to (b) and (c). Figs. (e) and (f) show an ultrasound image before and after needle insertion, respectively, where each mesh point is matched to a pixel in the image.

FEM and PHS, in which the needle is inserted into the mesh from different insertion points and different insertion depths. The errors from these three simulations form a fitness vector:

$$\mathbf{f}(\mathbf{x}) = [\mathrm{MAE}_1(\mathbf{x}),\, \mathrm{MAE}_2(\mathbf{x}),\, \mathrm{MAE}_3(\mathbf{x})]^\top, \qquad (24)$$

which is a function of vector $\mathbf{x}$ aggregating the model parameters from Table I. NSGA-II is then used to minimize $\mathbf{f}(\mathbf{x})$ and generate a Pareto front of optimal solutions across the three errors. From this set, a set of parameters is selected by choosing the solution with minimal error. The tuned parameter values are given in Table I.

V. Simulation Results

Fig. 2(a) shows a sample result of a needle insertion into the mesh (from the left side) using PHS. The tissue volume is represented as a normalized unit cube discretized on a $25 \times 25 \times 25$ grid. The needle enters at a fixed point and advances quasi-statically toward a prescribed target over 20 discrete steps; the figure shows the needle at the final insertion depth. At each step, localized target displacements are computed based on the model proposed in Section III. The PHS deformation is solved at every step as a mapping from the undeformed reference nodes to their accumulated target positions. Boundary conditions are enforced by fixing the external faces of the cube excluding the entry face. Once deformation is computed, the volume can be sliced along an arbitrary imaging plane such as the one highlighted in blue at $z = 0.5$ (The ultrasound probe is represented as the grey rectangle at the north face of the cube). All points on this imaging plane can then be plotted in 2D, with the needle trajectory projected onto the same plane for qualitative assessment. The location of ultrasound image pixels can then be matched to the location of each node in the 2D slice.

Fig. 2 (b) and (c) show another example of 2D slices obtained from a PHS and the equivalent FEM volumes. The error between the pairwise nodal displacements of the originating volume are summarized by the histogram in Fig. 2(d). The use case for slicing the deformed volume is shown in Fig2(e) and (f) where the slice shown in (a) is matched to an ultrasound image before and after needle insertion. As it can be seen in (f), the effect of tissue displacement can be simulated in the image using PHS.

With the optimized parameters, 5 different mesh sizes ranging from $25 \times 25 \times 25$ to $48 \times 48 \times 48$ nodes were constructed using the FEM and PHS models normalized in length, width, and height to 1. We computed the error between FEM and PHS and the computational time per simulation step. All simulations were implemented on an Intel i5 computer with 16 GB of RAM. Fig. 3 summarizes the error between the FEM model and the tuned PHS simulation, as well as the computational time per simulation step. Across all mesh resolutions, both MAE and RMSE increase with insertion depth. This is expected since deformations accumulate as the needle advances in the mesh. The error curve flattens toward the end of insertion, indicating that incremental deformation per step is less variable after stability is established. Across all tested mesh sizes, the errors remain in the order of 10^{-3}, demonstrating close agreement between the PHS displacement field and the FEM solution throughout the insertion trajectory.

The per-step computational time of FEM and PHS is compared in Fig. 3(b). While both FEM and PHS runtime increase with the number of mesh nodes, the FEM's runtime grows substantially faster, leading to an increasing runtime gap at higher resolutions. Over the tested range, PHS remains orders of magnitude faster than FEM at approximately 220 to 410 times faster, demonstrating that the proposed approach main-

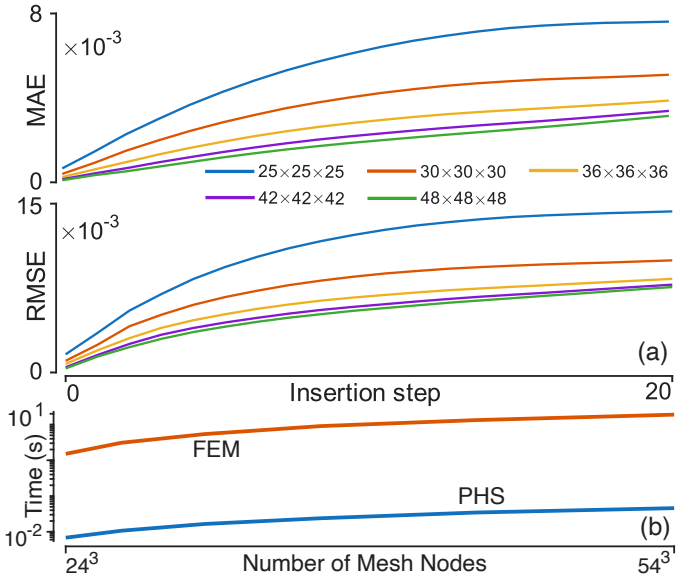

Fig. 3. MAE and RMSE between PHS and FEM across different mesh resolutions in (a), and per step simulation time (in logarithmic scale) as a function of the number of mesh nodes in the simulation in (b).

tains FEM-consistent deformation accuracy while enabling real-time performance as mesh resolution increases. Using the highest tested resolution, the PHS and FEM computational time were 45.8 and 18,919.7 milliseconds, respectively.

VI. Conclusion and Future Work

This paper presented a 3D PHS tissue deformation model to estimate tissue deformation during percutaneous surgery. Needle-tissue interaction is encoded through physically motivated displacement constraints capturing friction and tissue cutting that arise from needle insertion in the tissue. The resulting 3D PHS mapping produces a smooth deformation field over the volume, which may be sliced to produce a 2D deformed plane matching pixels in an ultrasound image. To validate the model against a standard FEM model, NSGA-II tuning was implemented to find the model parameters that minimized the error between FEM and PHS nodal displacements. This optimization produced a single Pareto optimal solution that was selected based on best global performance yielding the selected parameter values. Quantitative validation against a finite element reference implemented in FEniCSx showed that the proposed approach can closely reproduce FEM deformation trends while substantially reducing computational cost; up to 410 times in a 150,000 node mesh. Across multiple volumetric resolutions within a normalized unit-cube domain, the tuned PHS model maintained low displacement discrepancy relative to FEM and achieved large per-step speedups that increase with mesh resolution, supporting interactive update rates for volumetric simulation. In addition, the slicing mechanism provides a practical bridge between volumetric deformation and 2D ultrasound image generation by extracting and visualizing deformed grid planes aligned with typical probe sweeps.

Future work will focus on extending the model to more complex and patient-specific scenarios including heterogeneous tissue regions, and further decreasing computational expense with learning algorithms. We will also investigate how to improve parameter generalization across insertion sites and trajectories, and integrate relaxation and elastic effects to better capture time-dependent tissue response. Finally, the model will enable coupling mesh deformation fields to ultrasound image synthesis, and haptic force feedback in a training simulator.

References

[1] H. Mazdarani *et al.*, "Ultrasound-based visual servoing for out-of-plane longitudinal needle tracking in robot-aided percutaneous nephrolithotomy," *IEEE Access*, 2025.

[2] M. Trojak *et al.*, "Mixed Reality Biopsy Navigation System Utilizing Markerless Needle Tracking and Imaging Data Superimposition," *Cancers*, vol. 16, no. 10, p. 1894, 2024.

[3] H. Mazdarani *et al.*, "Integrating confidence maps and visual servoing for needle tracking in robotic us-guided percutaneous nephrolithotomy," *IEEE Open Journal of Instrumentation and Measurement*, 2025.

[4] B. Sainsbury *et al.*, "Preoperative virtual reality surgical rehearsal of renal access during percutaneous nephrolithotomy: A pilot study," *Electronics*, vol. 11, no. 10, p. 1562, 2022.

[5] Y. Song *et al.*, "Evaluating the learning curve for percutaneous nephrolithotomy under total ultrasound guidance," *PloS one*, vol. 10, no. 8, p. e0132986, 2015.

[6] B. Sainsbury *et al.*, "Evaluation of a virtual reality percutaneous nephrolithotomy surgical simulator," *Frontiers in Robotics and AI*, vol. 6, p. 145, 2020.

[7] A. Lelevé *et al.*, "Haptic training simulation," *Frontiers in virtual reality*, vol. 1, p. 3, 2020.

[8] C. Rossa and M. Tavakoli, "Issues in closed-loop needle steering," *Control engineering practice*, vol. 62, pp. 55–69, 2017.

[9] Y. Adagolodjo *et al.*, "Inverse real-time Finite Element simulation for robotic control of flexible needle insertion in deformable tissues," in *IEEE Inter. Conf. on Intell. Robots and Systems*, 2016, pp. 2717–2722.

[10] H. Mohammadi *et al.*, "Finite-Element Modelling of Needle-Tissue Interactions," *Archives of Computational Methods in Engineering*, vol. 31, no. 3, pp. 1363–1404, 2024.

[11] Y. Kobayashi *et al.*, "Development of an integrated needle insertion system with image guidance and deformation simulation," *Computerized Medical Imaging and Graphics*, vol. 34, no. 1, pp. 9–18, 2010.

[12] O. Goksel *et al.*, "Haptic simulator for prostate brachytherapy with simulated needle and probe interaction," *Transactions on haptics*, vol. 4, no. 3, pp. 188–198, 2011.

[13] B. Burger *et al.*, "Real-time gpu-based ultrasound simulation using deformable mesh models," *Transactions on medical imaging*, vol. 32, no. 3, pp. 609–618, 2012.

[14] L. Han *et al.*, "Fast deformation simulation of breasts using gpu-based dynamic explicit finite element method," in *Digital Mammography International Workshop*. Springer, 2010, pp. 728–735.

[15] H. Xie *et al.*, "Kalman filter finite element method for real-time soft tissue modeling," *IEEE Access*, vol. 8, pp. 53 471–53 483, 2020.

[16] W. Hou *et al.*, "A new model of soft tissue with constraints for interactive surgical simulation," *Computer Methods and Programs in Biomedicine*, vol. 175, pp. 35–43, 2019.

[17] M. Khadem *et al.*, "Mechanics of Tissue Cutting During Needle Insertion in Tissue," *Robotics and Automation Letters*, vol. 1, no. 2, pp. 800–807, 2016.

[18] K. Zalzalah *et al.*, "Real-Time Simulation of Ultrasound Image Deformation Using Thin Plate Spline," in *2025 IEEE Sensors Applications Symposium (SAS)*, Jul. 2025, pp. 1–6.

[19] C. Rossa *et al.*, "Nonlinear workspace mapping for telerobotic assistance of upper limb in patients with severe movement disorders," in *IEEE Inter. Conf. on Systems, Man, and Cybernetics*, 2017, pp. 2255–2260.

[20] H. P. Langtangen and A. Logg, *Solving PDEs in python: the FEniCS tutorial I*. Springer Nature, 2017.

[21] Y. Yusoff *et al.*, "Overview of nsga-ii for optimizing machining process parameters," *Procedia Engineering*, vol. 15, pp. 3978–3983, 2011.